Three epoch VLBI observations at 18 cm of low frequency variable sources

M. Bondi^{1,2}, L. Padrielli¹, R. Fanti^{1,3}, A. Ficarra¹, L. Gregorini^{1,3}, F. Mantovani¹, N. Bartel⁴, J.D. Romney⁵, G.D. Nicolson⁶, and K.W. Weiler⁷

- ¹ Istituto di Radioastronomia del CNR, Via Gobetti 101, I-40129 Bologna, Italy
- ² Nuffield Radio Astronomy Laboratories, Jodrell Bank, Cheshire, SK11 9DL, UK
- ³ Dipartimento di Fisica, Università di Bologna, Via Irnerio 46, I-40126 Bologna, Italy
- ⁴ Dept. of Physics and Astronomy, York University, 4700 Keele Street, North York, M3J 1P3, Canada
- ⁵ National Radio Astronomy Observatory, AOC, PO Box 0, Socorro, NM 87801, USA
- ⁶ Hartebeesthoek Radio Astronomy Observatory, PO Box 443, Krugersdorp, 1740, South Africa
- Center for Advanced Space Sensing, Naval Research Laboratory, Code 4215, Washington, DC 20375-5000, USA

Received 20 March 1995 / Accepted 1 August 1995

Abstract. We present third epoch VLBI observations at 1.67 GHz of a sample of 20 Low Frequency Variable Sources. The sources have been observed with a global array of 11 radio telescopes, recording in MK 2 mode, with a resolution of \sim 3 mas. We also present an analysis of possible variations in the fringe visibilities between an earlier epoch (1981.8) and the present epoch (1987.9), and compare these changes with those observed between the two epochs 1980.1 and 1981.8. Significant variations have been found in 17 out of 20 sources. In a number of cases the changes are clearly due to flux density variations in the most compact component. Several other cases appear to be due to either an increase in the angular size of a single component or a change in the angular separation between well defined components. Some sources show superluminal motions much like those usually observed at higher frequencies, and some new candidates for superluminal motions are identified. We have also used 408 MHz monitoring data, taken in the period of the VLBI observations, to derive an estimate of the Doppler factors necessary to account for the low frequency variability, and we compare these values with the Doppler factors calculated from the proper motions detected in our VLBI observations. This analysis confirms that two distinct phenomena, intrinsic superluminal beaming and extrinsic scintillation, are responsible for the low frequency variability seen in compact extragalactic radio sources.

Key words: quasars: general – BL Lacertae objects: general – galaxies: jets – radio continuum: galaxies

Send offprint requests to: M. Bondi, Istituto di Radioastronomia, Via Gobetti 101, I-40129 Bologna, Italy

1. Introduction

Compact extragalactic radio sources show flux density variations over a wide range of frequencies (see Altschuler 1989, Aller, Hughes and Aller 1991 for a review). The terms Low Frequency Variability (LFV) and High Frequency Variability (HFV) have been used in the past to describe the variability detected respectively at $\nu < 1$ GHz and $\nu > 1$ GHz. The LFV at 408 MHz has been studied in Bologna, using data from a large sample of sources observed monthly, for more than 10 years (Bondi et al., 1994b and references therein).

Analyses and interpretation of LFV in extragalactic radio sources (Spangler et al. 1993; Bondi et al. 1994b) have recently shown that most of the variability at 408 MHz is extrinsic and is due to refractive interstellar scintillation (RISS) in turbulent interstellar medium of our Galaxy (Shapirovskaya 1978, Rickett, Coles and Burgois 1984). The amplitude and timescale of the variability depend on the wavelength of observation, the angular size of the radio source, the physical and dynamical properties of the interstellar medium (the power spectrum and velocity dispersion of the density fluctuations) along the line of sight (Rickett 1990). The amplitude of the RISS variability increases at longer wavelengths and for more compact radio sources.

On the other hand, HFV is interpreted as being intrinsic and due to physical processes occurring inside the radio source, such as relativistic expansion of plasmoids emitting synchrotron radiation (but see Rickett et al. 1995 for an interpretation of the centimetre wavelength intraday variability of 0916+624). This variability is often associated with radio source components moving with superluminal velocities and rapid structure changes on VLBI scale. The related flux density variations drift to lower frequencies with decreasing amplitudes at increasing times with delays up to several years. Some low frequency variations drift to lower frequency up to several years.

ables apparently show both extrinsic RISS and intrinsic superluminal velocity related variations.

Determination of the spectral behaviour of an outburst is the best way to discriminate between the two phenomena but requires intensive multifrequency monitoring over several years (Padrielli et al. 1987, Mitchell et al. 1994). The observation of small scale structural changes combined with low frequency monitoring of the flux density variability represents an alternative test of the two origins.

To investigate these phenomena, a VLBI observing program on 21 low frequency variable sources (Fanti et al. 1981) was carried out at 1667 MHz in February 1980 (epoch 1, Romney et al. 1984, Paper I), and October 1981 (epoch 2, Padrielli et al. 1986, Paper II). Even over such a short time interval, significant structural changes were found in nine sources, probable changes in an additional four sources, and three new candidates for superluminal motions were proposed. A relationship between structural changes and spectral behaviour of the LFV was also established. Sources showing correlated LFV and HFV had structural changes, while sources showing no correlation between LFV and HFV did not.

To verify these results and to study the structure variations at 18 cm over a longer time interval, we obtained additional VLBI observations in November 1987 (epoch 3). Four sources (0607–157, 0723–008, 0859–140, and 1055+018) were also observed at an intermediate epoch (October 1982) which we will refer to as epoch 2.5.

2. Observations and data reduction

Third epoch observations were made at 1.667 GHz with MK2 recording system in standard setup during 48 hours on days 14-15 November 1987 (1987.9) with a global VLBI array of 12 telescopes: Effelsberg (Germany), Jodrell Bank (UK), Medicina (Italy), Onsala (Sweden), Simeiz (Crimea), Hartebeesthoek (South Africa), Green Bank (USA), Haystack (USA), Maryland Point (USA), North Liberty (USA), Fort Davis (USA), Owens Valley (USA). The Onsala radio telescope was discarded in the post-correlation analysis because of the low amplitude of the correlated fringes. The source list was the same as in Papers I and II but very strong solar interference made the data for 1504–166 useless. The sources were observed in snap-shot mode for a total time about two hours each. The same observing schedule (same GST intervals) as epochs 1 and 2 was employed to allow a more reliable determination of source visibility changes. The data were correlated using the Block 2 Correlator of the California Institute of Technology, and the raw data have been global fringe fitted in AIPS (Schwab and Cotton, 1983). Amplitude calibration was obtained by observing the calibrator sources 0440-003, 0851+202, 1404+286 and 2345-168, and deriving the antenna factors (Bondi et al. 1994a) separately for the North American and European subnetworks. A realistic estimate of the uncertainty in the overall amplitude calibration is of about 5%. The self-calibration mapping procedure has been performed in AIPS on the Convex C-210 of the "Istituto di Radioastronomia del CNR" in Bologna.

Table 1. Properties of the observed sources

Other Name	Id	m_V	Z	S_{tot}	S_{map}
				Jy	Jy
NRAO 091	Q	22.1		3.7	1.9
4C67.05	Q	19.0		1.5	1.3
	G	14.0	0.02	29.7	24.0
NRAO 140	Q	17.5	1.26	3.0	2.9
	Q	14.6	0.57	2.6	0.8
	BL	17.0	0.31	0.8	0.8
	Q	18.5	0.87	2.5	2.2
	Q	18.0	0.32	2.1	2.1
	G	18.0	0.13	2.1	1.7
	Q	16.5	0.19	2.2	2.1
OJ-140	Q	16.6	1.33	2.9	2.4
4C01.28	Q	18.3	0.89	2.9	2.6
4C12.39	Q	19.3	2.12	2.1	1.6
OM-146	Q	16.9	1.19	5.6	5.0
OR-102	Q	18.5	0.88		
OR-017	Q	16.5	0.36	1.8	1.5
DA406	Q	17.5	1.40	2.9	2.9
3C345	Q	16.0	0.60	9.6	8.0
NRAO530	Q	18.5	0.90	6.7	6.1
BL Lac	BL	14.7	0.07	2.8	2.5
3C545.3	Q	16.1	0.86	14.3	12.7
	NRAO 091 4C67.05 NRAO 140 OJ-140 4C01.28 4C12.39 OM-146 OR-102 OR-017 DA406 3C345 NRAO530 BL Lac	NRAO 091 Q 4C67.05 Q G NRAO 140 Q Q BL Q Q Q G Q OJ-140 Q 4C01.28 Q 4C12.39 Q OM-146 Q OR-102 Q OR-017 Q DA406 Q 3C345 Q NRAO530 Q BL Lac BL	NRAO 091 Q 22.1 4C67.05 Q 19.0 G 14.0 NRAO 140 Q 17.5 Q 14.6 BL 17.0 Q 18.5 Q 18.0 G 18.0 Q 16.5 OJ-140 Q 16.6 4C01.28 Q 18.3 4C12.39 Q 19.3 OM-146 Q 16.9 OR-102 Q 18.5 OR-017 Q 16.5 DA406 Q 17.5 3C345 Q 16.0 NRAO530 Q 18.5 BL Lac BL 14.7	NRAO 091 Q 22.1 4C67.05 Q 19.0 G 14.0 0.02 NRAO 140 Q 17.5 1.26 Q 14.6 0.57 BL 17.0 0.31 Q 18.5 0.87 Q 18.0 0.32 G 18.0 0.13 Q 16.5 0.19 OJ-140 Q 16.6 1.33 4C01.28 Q 18.3 0.89 4C12.39 Q 19.3 2.12 OM-146 Q 16.9 1.19 OR-102 Q 18.5 0.88 OR-017 Q 16.5 0.36 DA406 Q 17.5 1.40 3C345 Q 18.5 0.90 BL Lac BL 14.7 0.07	NRAO 091 Q 22.1 3.7 4C67.05 Q 19.0 1.5 G 14.0 0.02 29.7 NRAO 140 Q 17.5 1.26 3.0 Q 14.6 0.57 2.6 BL 17.0 0.31 0.8 Q 18.5 0.87 2.5 Q 18.0 0.32 2.1 G 18.0 0.13 2.1 Q 16.5 0.19 2.2 OJ-140 Q 16.6 1.33 2.9 4C01.28 Q 18.3 0.89 2.9 4C12.39 Q 19.3 2.12 2.1 OM-146 Q 16.9 1.19 5.6 OR-102 Q 18.5 0.88 OR-017 Q 16.5 0.36 1.8 DA406 Q 17.5 1.40 2.9 3C345 Q 16.0 0.60 9.6 NRAO530 Q 18.5 0.90 6.7 BL Lac BL 14.7 0.07 2.8

The relevant properties of the sources are listed in Table 1 and the maps are shown in Figs. 1-5. Optical identifications, visual magnitudes and redshifts are from Véron and Véron (1991), Hewitt and Burbidge (1987), and Stickel, Meisenheimer and Kühr (1994); S_{tot} is the single dish flux density measured by the Effelsberg antenna, S_{map} is the total flux density in the VLBI map. The adopted "restoring beams" are the same as those used in the previous epoch maps.

3. Comparison between the epochs

Even using the same observing schedule for the three epochs, the data have different sensitivity and slightly different u-v coverage because of some different telescopes observing at each run. Furthermore, for most of the sources the u-v coverage is poor, which can introduce additional uncertainties in the map parameters. Thus, the comparison between maps at different epochs cannot be considered the crucial test for detecting changes in the source structure by itself. The comparison between the amplitudes and the closure phases of the fringe visibilities at the different epochs is more reliable, so we used the same analysis as in Paper II:

1. A preliminary search of sources having significant variations between epochs 2 and 3 was done using a χ^2 test on the amplitudes of the fringe visibilities. The amplitudes were individually averaged within boxes of 0.25 M λ in the u-v-plane in order to increase the signal-to-noise ratio in the data, and then compared between the two epochs, using a

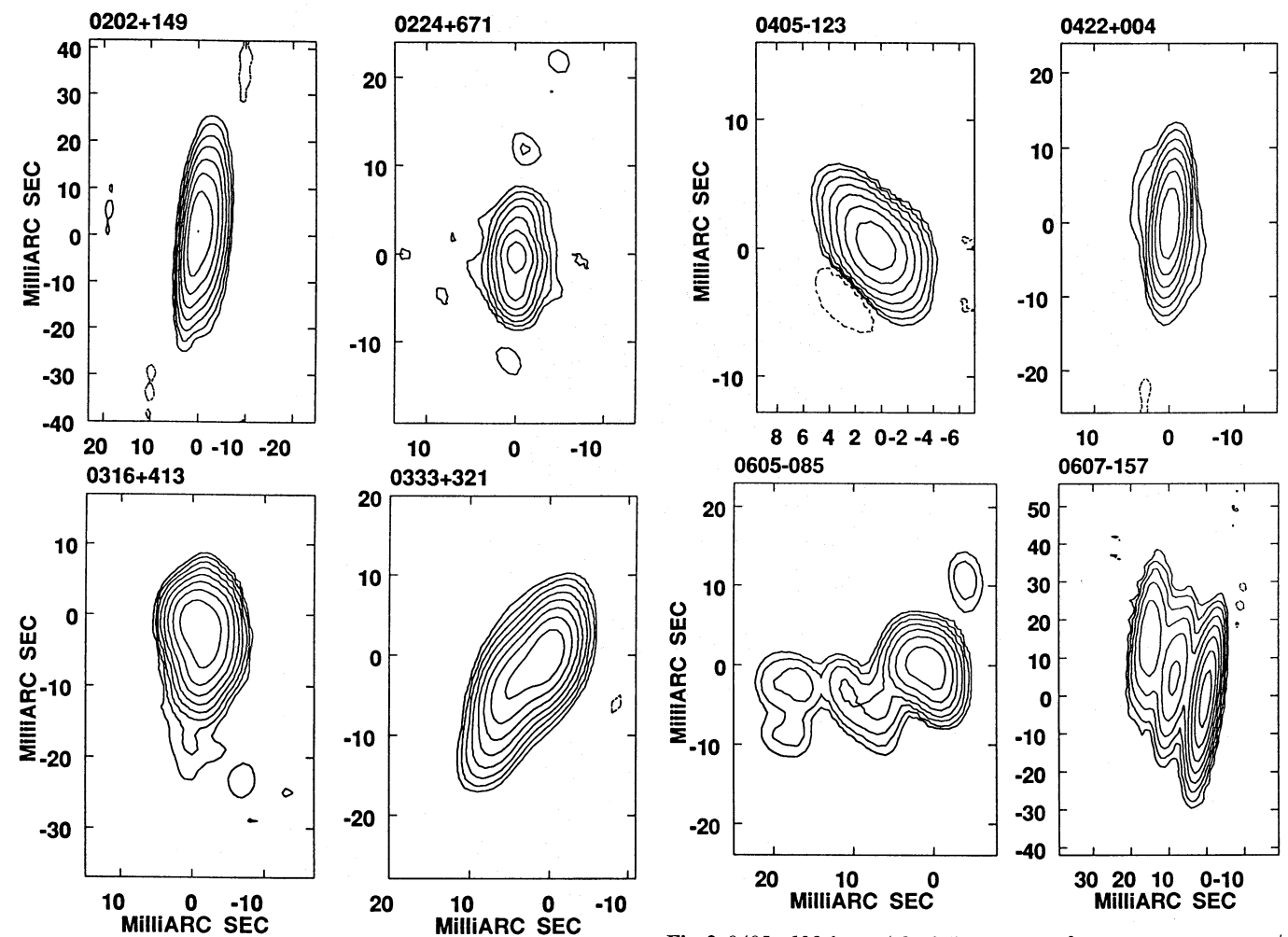


Fig. 1. 0202+149: beam 18.0×2.5 mas $p.a.-5^{\circ}$, peak 1.02 Jy/beam, 1^{st} contour 8 mJy/beam. 0224+671: beam 3.5×2.5 mas $p.a.-9^{\circ}$, peak 0.69 Jy/beam, 1^{st} contour 7 mJy/beam. 0316+413: beam 5.0×3.0 mas $p.a.-5^{\circ}$, peak 7.23 Jy/beam, 1^{st} contour 30 mJy/beam. 0333+321: beam 6.5×3.0 mas $p.a.-11^{\circ}$, peak 1.19 Jy/beam, 1^{st} contour 5 mJy/beam. Levels are -1, 1, 2, 4, 8, 16, 32, 64, 128, 256, 512, 1024 times the 1^{st} contour.

Fig. 2. 0.405-123: beam 4.0×2.5 mas p.a. 32° , peak 0.53 Jy/beam, 1^{st} contour 5 mJy/beam. 0.422+0.04: beam 10.0×2.5 mas p.a. -5° , peak 0.66 Jy/beam, 1^{st} contour 5.4 mJy/beam. 0.605-0.85: beam 4.5×3.0 mas p.a. 19° , peak 0.87 Jy/beam, 1^{st} contour 8 mJy/beam. 0.607-157: beam 20.0×3.0 mas p.a. -8° , peak 1.10 Jy/beam, 1^{st} contour 6 mJy/beam. Levels are -1, 1, 2, 4, 8, 16, 32, 64, 128, 256, 52, 1024 times the 1^{st} contour.

 χ^2 analysis:

$$\chi^2 = \sum_{i=1}^{N} \frac{[A_i(3) - A_i(2)]^2}{\sigma_{i,comb}^2}$$
 (1)

 $A_i(2)$ and $A_i(3)$ are the average values of the amplitudes in the *ith* box for epochs 2 and 3, respectively. The combined error is defined as:

$$\sigma_{i,comb}^2 = \sigma_i^2(3) + \sigma_i^2(2) + [0.10A_i(3)]^2 + [0.10A_i(2)]^2 \eqno(2)$$

where $\sigma_i(2)$ and $\sigma_i(3)$ are the standard noise errors, and 0.10 is a conservative estimate of the flux density scale error, taking into account both gain variations on short temporal scales and residual calibration errors.

The closure phases at the two epochs were examined in a similar manner but, since the coincident points for closure

triangles are very few, this test has little weight in the analysis.

We then tried to relate the fringe visibility variations to changes in the source structure using both model-fitting of the visibilities and multi-component gaussian fitting to the maps.

We also compared the fringe amplitudes at different epochs, along position angles selected on the basis of the source structure, when there is good u-v coverage, or on the basis of the available u-v coverage for the more poorly sampled sources. We fitted these amplitudes with one-dimensional, simple source models as in Paper II. This analysis is independent of the CLEAN procedure, and makes it possible to verify if the observed variations are real or just caused by a different u-v coverage and/or different sensitivity of the array.

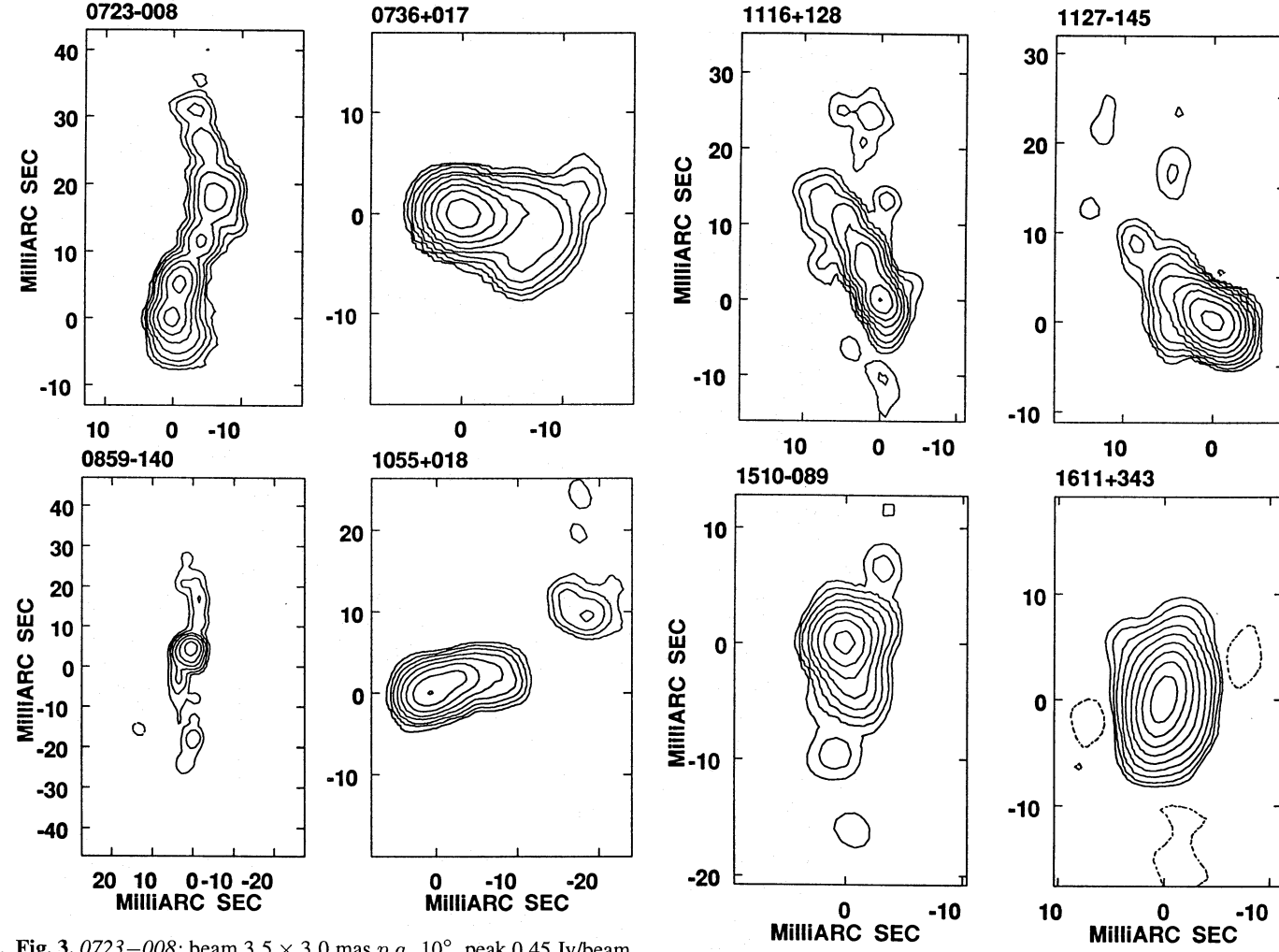


Fig. 3. 0723-008: beam 3.5 \times 3.0 mas p.a. 10°, peak 0.45 Jy/beam, 1^{st} contour 5 mJy/beam. 0736+017: beam 3.5 \times 3.0 mas p.a. 36°, peak 1.33 Jy/beam, 1^{st} contour 3 mJy/beam. 0859-140: beam 3.5 \times 3.0 mas p.a. 48°, peak 0.97 Jy/beam, 1^{st} contour 20 mJy/beam. 1055+018: beam 3.0 \times 2.5 mas p.a. 69°, peak 0.79 Jy/beam, 1^{st} contour 6 mJy/beam. Levels are -1, 1, 2, 4, 8, 16, 32, 64, 128, 256, 512, 1024 times the 1^{st} contour.

Some plots of the visibilities along selected ranges in position angle at different epochs are shown in Sect. 5. The data for the four sources observed at epoch 2.5 have been used at this stage to detect any continuity in the observed structural changes.

4. Results

The results of the χ^2 analysis between epochs 1 and 2, and between epochs 2 and 3 are summarized in Table 2. The values of the reduced χ^2 ($\chi^2_{\nu}=\chi^2/(N-1)$), are listed in columns 3 to 7 with the corresponding number of degrees of freedom (N-1) in parentheses. It is important to note that the number of independent points is the number of u-v boxes and not the number, approximately 4 or 5, of u-v measurements within each box. Column 3 is the χ^2_{ν} , calculated using all the data. Columns 4 and 5 list the χ^2_{ν} calculated using only baselines greater and smaller

Fig. 4. 1116+128: beam 3.0×2.5 mas p.a. 26° , peak 0.60 Jy/beam, 1^{st} contour 4.5 mJy/beam. 1127-145: beam 3.5×2.5 mas p.a. 32° , peak 2.63 Jy/beam, 1^{st} contour 8 mJy/beam. 1510-089: beam 3.0×2.5 mas p.a. 26° , peak 1.02 Jy/beam, 1^{st} contour 6 mJy/beam. 1611+343: beam 5.0×2.5 mas p.a. -13° , peak 2.06 Jy/beam, 1^{st} contour 5 mJy/beam. Levels are -1, 1, 2, 4, 8, 16, 32, 64, 128, 256, 512, 1024 times the 1^{st} contour.

than $20M\lambda$, respectively. The value of $20M\lambda$ corresponds to about half the maximum baseline. For baselines greater than $20M\lambda$ we have also calculated the χ^2_ν for baselines in the North–South direction (position angle $\theta=0^\circ\pm20^\circ$; column 6), and in the East–West direction (position angle $\theta=90^\circ\pm20^\circ$; column 7). Values of χ^2_ν with less than 3 degrees of freedom have not been considered. High χ^2_ν produced by only one data point or by one baseline are not considered significant and are discarded from the analysis. The last column of Table 2 lists the result of the analysis: V, P, and N stands, respectively, for variable, probably variable and not variable. Following Paper II, if the probability is p<0.1% that the variability is produced by random fluctuations in the errors we define the source as "V". If the probability is 0.1% we define it as "P". Otherwise it is "N".

Table 2. Analysis of the χ_{ν}

Name	epoch	$\chi^2_{ u}$	$b < 20 M\lambda$	$b > 20~M\lambda$	$b > 20~M\lambda$	$b > 20~M\lambda$	Var
					$ heta\sim0^{\circ}$	$ heta \sim 90^\circ$	
0202+149	1980-81	4.2 (26)	1.3 (19)	13.8 (6)		14.5 (5)	V
	1981-87	4.2 (58)	2.3 (24)	5.6 (33)	2.6 (16)	10.5 (9)	V
0224+671	1980-81	6.1 (53)	1.9(31)	12.7(21)	22.2(9)	1.5(4)	V
	1981-87	2.5 (22)	2.0 (16)	3.8 (6)			V
0316+413	1980-81	1.4 (33)	0.7 (17)	2.3 (15)	0.2 (4)	4.4 (5)	P
	1981-87	7.2 (27)	4.2 (14)	10.4 (14)	6.8 (4)		V
0333+321	1980-81	1.1 (42)	0.9 (23)	1.3 (18)	1.0 (5)	1.8 (9)	N
	1981-87	3.9 (68)	1.2 (34)	6.6 (34)	12.5 (12)	4.6 (20)	V
0405 - 123	1980-81	1.5 (19)	1.3 (11)	2.1 (7)	2.5 (4)	<u> </u>	N
	1981-87	2.7 (22)	3.0 (12)	2.3 (11)	0.9 (6)	_	V
0422+004	1980-81	0.7 (27)	0.5 (13)	0.9 (13)	0.8 (5)	1.0 (3)	N
	1981-87	5.3 (27)	4.9 (15)	5.7 (12)	6.3 (4)		V
0605-085	1980-81	4.0 (25)	3.5 (14)	3.5 (10)	4.0 (4)	3.0 (5)	V
	1981-87	20.4 (18)	10.6 (9)	32.7 (8)	33.9 (5)		V
0607-157	1980-81	11.6 (10)	9.6 (5)	17.0 (4)	_	15.3 (3)	\mathbf{v}
	1981-87	30.7 (22)	24.8 (13)	32.2 (9)	35.8 (6)	· · ·	V
0723008	1980-81	1.0 (30)	0.5 (13)	1.6 (16)	1.6 (8)	2.0 (5)	N
	1981-87	1.6 (28)	1.4 (13)	1.9 (15)	1.1 (7)	5.2 (3)	N
0736+017	1980-81	2.4 (28)	1.1 (11)	3.4 (16)	3.5 (8)	4.6 (5)	V
	1981-87	13.9 (33)	3.5 (14)	21.6 (19)	34.9 (9)	2.6 (6)	V
0859 - 140	1980-81	1.5 (19)	0.8 (10)	2.6 (8)	0.6 (4)	5.7 (3)	N
	1981-87	1.0 (26)	0.6 (17)	1.8 (9)	2.0 (8)	_	N
1055+018	1980-81	1.1 (29)	0.3 (16)	2.3 (12)	1.8 (4)	2.6 (6)	P
	1981-87	3.5 (36)	0.9 (23)	8.4 (13)	2.3 (8)	29.4 (3)	V
1116+128	1980-81	1.5 (36)	0.6 (19)	2.6 (16)	2.1 (7)	2.9 (9)	P
	1981-87	5.2 (34)	1.8 (19)	9.4 (15)	13.7 (8)	7.2 (4)	V
1127-145	1980-81	1.1 (15)	1.3 (8)	1.0 (6)	` <u>-</u>	_	N
	1981-87	3.4 (14)	1.5 (6)	4.8 (8)	0.8 (5)	_	V
1510-089	1980-81	3.6 (19)	1.4 (9)	6.2 (9)	13.3 (4)	1.0 (4)	V
	1981-87	6.7 (29)	5.1 (14)	8.3 (15)	18.1 (4)	4.8 (9)	V
1611+343	1980-81	0.9 (40)	0.6 (22)	1.2 (17)	0.3 (6)	2.0 (9)	N
	1981-87	1.1 (33)	0.3 (17)	2.1 (16)	1.3 (8)	1.4 (15)	N
1641+399	1980-81	6.1 (39)	0.9 (20)	12.5 (18)	11.1 (10)	12.1 (7)	V
	1981-87	9.5 (25)	3.6 (11)	11.8 (18)	2.7 (6)	15.3 (7)	V
1730-130	1980-81	6.0 (24)	4.8 (15)	9.1 (8)	14.7 (3)	4.5 (4)	V
	1981-87	19.3 (37)	11.1 (17)	27.1 (18)	28.5 (13)	11.6 (3)	V
2200+420	1980-81	32.0 (43)	34.0 (26)	34.4 (16)	23.0 (3)	28.1 (7)	V
	1981-87	17.4 (43)	12.3 (19)	21.5 (24)	23.7 (7)	10.4 (11)	v
2251+151	1980-81	0.9 (47)	0.5 (23)	1.4 (23)	3.4 (7)	0.6 (15)	P
	1981-87	15.4 (67)	10.9 (33)	19.7 (34)	30.2 (15)	8.9 (14)	V
	1701 07	15.7 (07)	10.7 (33)	17.7 (34)	30.2 (13)	0.2 (17)	

Table 2 shows that:

- 1. 17 out of 20 sources (85%) can be classified as variable between epochs 2 and 3, compared to the 9 variable (45%) and 4 probably variable (20%) between epochs 1 and 2.
- 2. Among the 7 sources (35%) found not variable between epochs 1 and 2 (time interval of almost 2 years), only 3 (17%) are still not variable between epochs 2 and 3 (time interval of about 6 years). All sources found variable between epochs 1 and 2 are also variable between epochs 2 and 3.
- 3. Comparison between the values in columns 4 and 5 shows that the probability of detecting significant variations greatly

- increases with baseline length, implying that most variations occur on the smallest angular size scales, as expected.
- 4. Comparison between the χ^2_{ν} obtained for the two time intervals at different position angles shows that, statistically, each source tends to vary along a preferred position angle, i.e. sources showing higher values of χ^2_{ν} along position angle, for instance, $\sim 0^{\circ}$ between epochs 1 and 2, still have higher values of χ^2_{ν} along the same position angle between epochs 2 and 3.

Fig. 6 shows the distribution of the global χ^2_{ν} obtained between epochs 1 and 2, and epochs 2 and 3. It is clear that the longer time interval between epochs 2 and 3 has the effect of

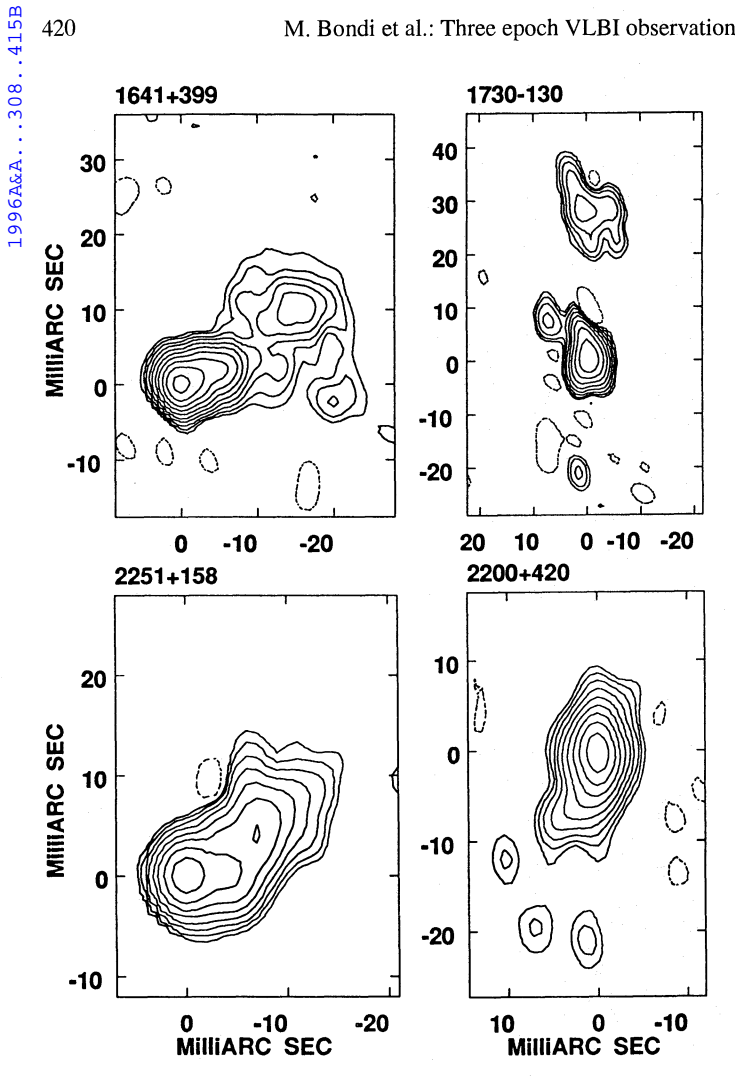


Fig. 5. 1641+399: beam 3.5×2.5 mas p.a. 14°, peak 3.43 Jy/beam, 1^{st} contour 5 mJy/beam. 1730-130: beam 4.5×2.5 mas p.a. 12° , peak 2.47 Jy/beam, 1^{st} contour 10 mJy/beam. 2251+151: beam 4.0×3.0 mas $p.a. 0^{\circ}$, peak 5.10 Jy/beam, 1^{st} contour 24 mJy/beam. 2200+420: beam 3.5×2.5 mas $p.a.5^{\circ}$, peak 1.31 Jy/beam, 1^{st} contour 3 mJy/beam. Levels are -1, 1, 2, 4, 8, 16, 32, 64, 128, 256, 512, 1024 times the 1st contour.

increasing the values of the calculated χ^2_{ν} . This implies that the timescale of the variability is generally greater than the 2 years interval between epochs 1 and 2. The 6 years between epochs 2 and 3 are sufficient to reveal variations in almost all of the observed sources.

The maps obtained from the epoch 3 data set have been fitted with multiple elliptical gaussian components using the task JMFIT in AIPS. It must be kept in mind that the sparse u-v coverage of the low declination sources can produce unreal features during hybrid mapping, and extended emission in the N-S direction must be taken with caution. We have therefore used model-fitting techniques on the u-v data to check the reliability of the parameters derived from the images.

Table 3 contains the results of these fits together with those from earlier epochs. The terminology for source components in Table 3 is: C – the central component, assumed to contain the core; J - a jet-like component; E - an extended or halo-like component; O – an old component detected in a previous epoch map but not in the last epoch; N – new component observed only in the epoch 3 map; A and B - other components detected at all the epochs. For each component and each epoch, Table 3 lists its flux density at 18 cm (S), its polar coordinate position (r in mas and p.a. in degrees from N to E) with respect to the first component, and its FWHM angular size (major and minor axes in mas) and position angle (p.a. of the major axis in degrees from N to E). For extended or narrow, jet-like, features it was difficult to obtain reliable fits. In these cases, instead of giving the FWHM of the components, we indicate the total extension of the component and its position angle.

Comparing the results of the different fitting procedures, we have derived error estimates for the flux density of $\simeq 10\%$ of the peak brightness of the radio components, and for source dimension of $\simeq 20\%$ of the beam size for small angular sizes or angular separations. For extended components the error is much larger.

The last column contains a code used to classify the observed variability between the last two epochs.

- 1. F: flux density variability of one or more components, without any evidence of structural variations. Five sources (0202+149, 0333+321, 0422+004, 1510-089, and 1730–130) show changes which can be interpreted in terms of flux density variations of components without separation and component size changes.
- 2. S: flux density variability associated with separation change or with expansion of known components between epochs 2 and 3, or with the appearance of a new component. Six sources (0224+671, 0605–085, 1055+018, 1641+399, 2200+420 and 2251+158) are classified in this category.
- 3. C: complex variations with flux density and structural changes which cannot be associated in a simple way with components seen at both epochs. Six sources (0316+413, 0405-123, 0607-157, 0736+017, 1116+128,and 1127–145) belong to this category.
- 4. N: sources without significant variations in flux density or morphology (0723–008, 0859–140, and 1611+343).

5. Comments on individual sources

In this section we give a simple description of the brightness distribution for each source as was derived by various fitting techniques, a summary of the variability observed from the three epochs, and some comments.

0202+149: well fitted by a two component model. The separation and dimensions of the two components did not change significantly over the three epochs. On the other hand, both components show strong ($\sim 40\%$) flux density variability.

The source is unresolved by the VLA at 1.4 GHz (Perley 1982) and by MERLIN at 408 MHz (Mantovani, private communication), but the VLBI map accounts only for $\sim 50\%$ of the flux density measured by the Effelsberg 100 m telescope. This means that there must be an extended component on a scale of hundreds of mas completely resolved by our observations.

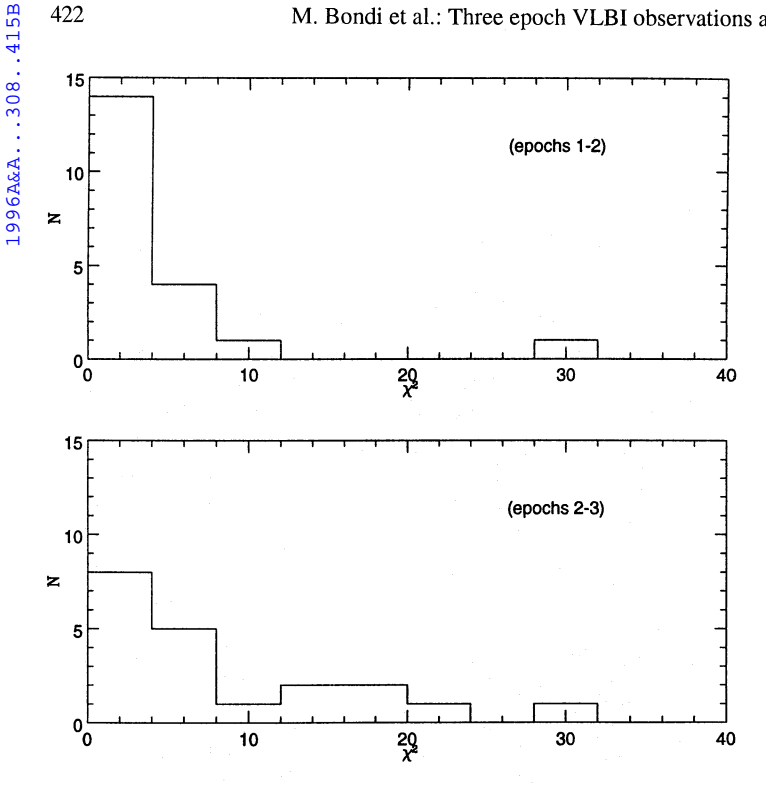
Table 3. Source parameters

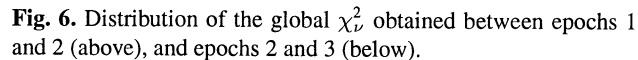
	Epoch 1: 1980.1						Epoch 2: 1981.8					Epoch 3: 1987.9								
Name	Comp.	S	r	p.a.	maj	min	p.a.	S	r	p.a.	maj	min	p.a.	S	r	p.a.	maj	min	p.a.	
0202+149	Α	0.8 ± 0.1			4.0 ± 1.6	0.9 ± 0.5	162	1.4±0.1			4.0±1.6	1.3±0.5	172	1.4±0.1			2.8±0.5	1.1±1.6	82	
	В	1.2±0.1	3.2±0.5	281	5.0 ± 1.6	1.8 ± 0.6	150	0.9±0.1	3.7 ± 0.6	294	5.5 ± 3.6	1.2 ± 0.5	182	0.6±0.1	3.3 ± 0.6	292	4.5 ± 3.6	1.9 ± 0.5	185	r
0224+671	C	1.1 ± 0.1			2.8±0.6	1.3±0.6	180	0.9±0.1			3.7±0.6	1.0±0.6	171	1.3±0.1			5.7±0.6	1.4±0.6	177	
	0	0.2±0.1	6.6 ± 0.5	357	~ 1	0±1	346				-									5
0316+413	\mathbf{C}	9.7 ± 0.6			4.1 ± 0.8	3.0 ± 0.9	42	9.0±0.7			4.3±0.8	2.4±0.9	42	8.7±0.9			3.4±1.0	2.4±0.6	0	
	E	6.5±0.6	0.0 ± 0.1	0	13±1	3.5 ± 0.6	175	8.9±0.7	0.0 ± 0.1	. 0	11±1	3.7 ± 0.6	171	15.0±1.0	$3.0\!\pm\!1.0$	240	9.0 ± 1.0	3.0 ± 0.6	180	C
0333+321	C	1.3 ± 0.1			$3.5\!\pm\!1.0$	0.5 ± 0.8	130	1.2±0.1			3.0 ± 1.0	1.2±0.8	139	1.5±0.1			3.1±1.0	1.5±0.8	127	E
	A	1.6±0.1	6.4±1.0	133	5.5 ± 1.0	0.5 ± 0.8	133	1.8±0.1	5.9 ± 1.0	129	6.5 ± 1.0	1.4 ± 0.8	151	1.3±0.1	$5.9\!\pm\!1.0$	130	6.2 ± 1.0	1.8 ± 0.8	138	Г
0405-123	С	1.0±0.1			4.7±0.8	1.0 ± 0.5	18	0.8±0.1			4.6 ± 0.8	1.2 ± 0.5	14	0.8±0.1			3.1±0.8	1.9±0.6	27	C
0422+004	С	1.1±0.1			1.9±0.8	0.6 ± 1.0	46	1.1±0.1			2.0 ± 0.8	0.5 ± 1.0	33	0.8±0.1			1.8±0.8	0.6±1.0	26	F
0605-085	C	2.2 ± 0.1			4.0 ± 0.8	3.5 ± 0.7	46	2.8±0.1			5.0 ± 0.9	2.5±0.6	30	1.9±0.1				3.9±0.6	29	
	J	0.4 ± 0.1			~]	12±1	150	0.3±0.1			~ 1	1±1	170	0.2±0.1	8.0 ± 1.0	125	4.0 ± 1.0	2.0 ± 1.0	25	S
														0.1±0.1	16±1	100	10 ± 1.0	5 ± 1	17	
0607-157	C	0.9 ± 0.1			6±2	4.0 ± 0.6	7	0.6±0.1			7±2	7.0±0.6	0	1.3±0.1			2±1	2±1	49	
	N													0.5±0.1	21±2	46	6±1	6±1	- 0	
	J	0.5±0.1			~ :	25±3	40	0.5 ± 0.1			~ 2	5±3	37	0.4±0.1	9±2	59	5±1	4±1	36	C
0723-008	C	0.2 ± 0.1			2.5 ± 0.6	0.5 ± 0.6	82	0.3±0.1			2.9 ± 0.6	$0.5{\pm}0.6$	60	0.4±0.1			3.1 ± 0.7	1.7±0.6	157	
	Α	1.2 ± 0.1	2.5 ± 1.0	349	$7.7\!\pm\!1.0$	1.6 ± 1.0	344	1.2±0.1	3.5 ± 1.0	352	7.6 ± 1.0	$2.0\!\pm\!1.0$	361	1.7±0.1			~ 2	5±2	345	N
	В	0.7±0.1	16±2	340	~	6±1	345	0.6±0.1	17±2	340	5±1	4±1	345					·		
0736+017	Α	0.6 ± 0.1			1.5 ± 0.7	0.5 ± 0.7	49	0.4±0.1			2.1 ± 0.7	$0.5{\pm}0.7$	76	1.5±0.1			1.6±0.6	0.6 ± 0.7	96	
	N													0.4±0.1	3.0 ± 0.6	263	1.5 ± 0.7	1.1 ± 0.7	147	
	В	1.8±0.1	6.0±0.7	277	3.2±0.7	2.5±0.7	110	1.5±0.1	6.0 ± 0.7	271	3.0 ± 0.7	2.5 ± 0.7	45	0.3 ± 0.1	6.0 ± 0.6	260	~ 1	0±1	100	\mathbf{C}
0859-140	C	1.6 ± 0.1			~	6±1	160	1.5±0.1			~ :	5±1	170	1.6±0.1			~	4±1	168	
	Α	0.4 ± 0.1	10±2	356	~ 1	14±2	25	0.3±0.1	8±2	352	~1	5±2	175	0.3±0.1	8±2	350	~ 1	5±2	174	N
	В	0.6 ± 0.1	11±2	174	~ 2	20±2	22	0.5±0.1	12±2	171	~ 2	0±2	178	0.5±0.1	14±2	180	~ 1	8±2	177	

Table 3. (continued)

1055+018	С	1.9±0.1			4.9±0.6	1.9±0.6	130	1.9±0.1			5.0±0.6	1.8±0.6	124	1.0±0.1			2.6±0.6	1,5±0.6	110	
	N1													1.2±0.1	2.8 ± 0.6	296	5.2 ± 0.6	1.9 ± 0.6	101	
	0	0.3 ± 0.1	4.0 ± 0.6	40	3.8 ± 0.6	2.8 ± 0.6	40	0.3±0.1	3.9 ± 0.6	43	3.5 ± 0.6	2.5 ± 0.6	81							S
	A	0.2 ± 0.1	8.1±0.6	308	3.0 ± 0.6	2.7 ± 0.6	107	0.3±0.1	8.0 ± 0.6	307	3.5 ± 0.6	2.6 ± 0.6	105	0.2±0.1	9.0 ± 0.6	290	4.3 ± 0.6	2.0 ± 0.6	100	
	N2													0.1±0.1	21±2	297	5.3 ± 0.6	3.0 ± 0.6	60	
1116+128	C	0.9 ± 0.1			4.0 ± 0.7	1.5 ± 0.7	32	0.7±0.1			5.0 ± 0.7	1.7±0.7	22	0.7±0.1			1.8±0.7	0.9±0.7	26	
	N													0.8±0.1	5.7 ± 0.7	23	5.4 ± 0.7	2.2 ± 0.7	24	C
	E	0.4 ± 0.1			13±2	3±1	27	0.3±0.1			15 ± 2	3±1	25	0.2±0.1			25 ± 2	3±1	25	
1127+145	C	2.5 ± 0.2			3.4 ± 0.5	0.5±0.6	. 89	2.1±0.2			3.6±0.5	0.5±0.6	80	3.3±0.2			1.8±0.5	1.2±0.6	77	
	E	2.8 ± 0.2	$2.3\!\pm\!1.0$	4	9.9 ± 2.0	3.6 ± 0.6	- 20	2.7±0.2	2.9 ± 1.0	10	8.0 ± 2.0	3.6 ± 0.6	25	1.9±0.2	3.3 ± 1.0	50	6.7 ± 2.0	1.8±0.6	50	С
1510-089	C	2.4±0.2			1.4±0.5	0.8±0.5	305	2.1±0.1			2.0±0.5	0.7±0.5	333	1.3±0.1			1.9±0.5	1.0±0.5	139	
	J	0.3 ± 0.2			~ 6.0	~ 6.0±0.6 180		0.4±0.1			~ 6.0±0.6 180		0.2±0.1			~ 6.0±0.6		180	F	
1611+343	C	2.4±0.2			3.1±0.8	1.8±0.6	141	2.6±0.2			3.1±0.8	1.8±0.6	156	2.8±0.2			2.8±0.8	1.2±0.6	165	N
1641+399	C	3.8±0.3			2.2±0.5	1.0±0.6	88	3.9±0.3			3.0±0.5	2.0±0.6	78	4.8±0.3	******		1.8±0.5	1.8±0.6		
	N													1.2±0.1	2.5 ± 0.5	285	2.2 ± 0.6	1.5±0.6	62	
	Α	1.4 ± 0.3	2.8 ± 0.5	290	1.9 ± 0.6	0.5 ± 0.5	43	1.0±0.2	3.3 ± 0.5	290	1.8±0.6	0.5 ± 0.5	44	1.7±0.2	5.3 ± 0.5	293	4.1±0.6	2.0±0.6	98	S
	E							0.2±0.1	15±1	300	~ 5	±2±		0.5±0.1	18±1	303	~ 1	0±2		
1730-130	C	2.9±0.2			4.7±0.9	1.0±0.5	27	2.4±0.1			5.7±0.9	2.0±0.5	3	4.7±0.2			3.2±0.8	2.0±0.5	43	
	Α	1.5 ± 0.2	25±5	0	~ 1	3±2	. 0	1.0±0.1	25±5	0	~ 1	3±2	0	1.2±0.2	25±5	0	~ 1	0±2	0	F
	В	0.5±0.2	20±5	180	~ 1	0±2	180	0.4±0.1	20±5	180	~	7±2	180	0.5±0.2	20±5	180				
2200+420	C	0.9±0.2			2.1±0.7	0.5±0.5	- 11	3.2±0.1			2.1±0.7	1.4±0.5	13	2.3±0.2			4.6±0.7	2.1±0.5	176	
	J	0.8 ± 0.1			9±1	3±1	348	0.9±0.2	2.8±0.6	152	9±1	3±1	354	1	6.2±0.7	161	4±1	2±1	0	S
2251+151	C	2.6±0.3			2.3±0.6	0.7±0.6	158	2.7±0.3			1.6±0.6	0.5±0.6	171	5.5±0.4			1.4±0.6	0.4±0.6	98	
	N														4.0±0.6	270	4.7±0.6	2.6±0.6	138	S
	Α	5.3±0.3	6.2±0.7	295	4.5±0.6	2.0±0.6	123	5.9±0.3	6.6+0.7	208	5.5±0.6	25+06	134	i	7.5±0.7	299	5.6±0.6	2.9±0.6	159	.,







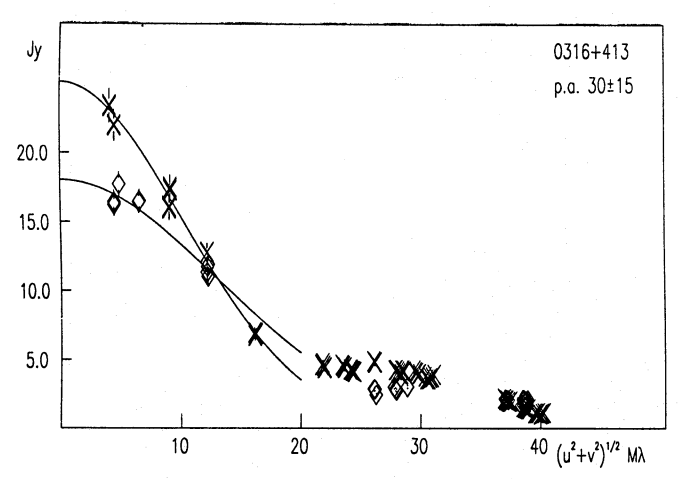


Fig. 7. Plot of amplitudes versus baseline length in a direction nearly parallel to the major axis of the source 0316+413. Diamonds refer to epoch 2 amplitudes and crosses to epoch 3.

0224+671: single component elongated in the N-S direction. The source size increased steadily from the first to the second epoch and from the second to the third. Comparison of the dimension along the N-S direction between the last two epochs, where we have more data, yields to an expansion rate of $\mu \simeq 0.3$ mas/yr.

On the arcsecond scale the source shows two lobes aligned with the mas extension (Perley, Fomalont & Johnston 1982, Mantovani private communication).

0316+413 (3C 84): complex structure on the longer baselines, and reasonably well fitted with a core-halo model on the shorter ones. Fig. 7 is a plot of the amplitudes in a position angle of 30° (the direction of best u-v coverage which is nearly along the ma-

jor axis) for the last two epochs. Baselines shorter than $20M\lambda$ have been fitted with a single gaussian component in order to obtain the overall dimensions of the source along p.a.= 30°. The fit shows that the angular dimension of 3C 84 clearly increased $(\theta_2 = 6.09 \pm 0.20 \text{ mas}, \theta_3 = 7.66 \pm 0.07 \text{ mas})$ in this direction. This corresponds to an expansion rate of ~ 0.3 mas/year consistent with a value of ~ 0.5 mas/year measured for the inner components (Marr et al. 1989, Venturi et al. 1993). The parameters in Table 3 also show this expansion with a displacement of 3 mas in p.a. 240° of component E.

0333+321: core-jet structure fitted with two components. We do not observe any significant variation in the extension or the separation of the two components, while the flux density of both changed between the last two epochs. This is a well known superluminal source on a smaller scale at higher frequencies (Marscher and Broderick 1985).

0405-123: single component. This source did not significantly vary between the first two epochs. The epoch 3 map does not confirm the presence of a N-S extension observed in the previous map. The χ^2_{ν} analysis shows that the flux density has varied uniformly on the shorter baselines as well as on the longer ones.

0422+004: compact. The source has remained unresolved while the flux density has decreased from 1.1 Jy to 0.8 Jy between epochs 2 and 3. It was constant between the first two epochs.

0605–085: core-jet structure. The large scale structure (> 10 mas) detected in epoch 3 is clearly produced by the better sensitivity of these observations compared to the previous epochs. An estimate of the variations on a small scale structure (< 10 mas) was performed by analysing the fringe amplitudes along p.a. 90° (Fig. 8). The epoch 2 data are compatible with a single component. The epoch 3 amplitudes show a minimum at $31M\lambda$

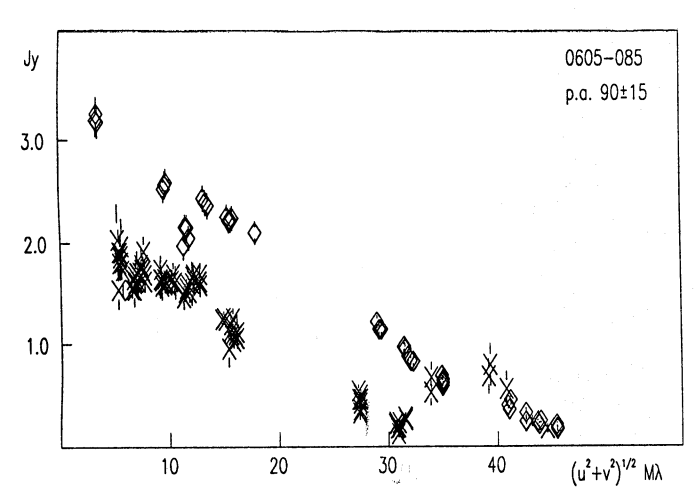


Fig. 8. Plot of amplitudes versus baseline length in position angle 90° for the source 0605-085. Diamonds refer to epoch 2 amplitudes and crosses to epoch 3.

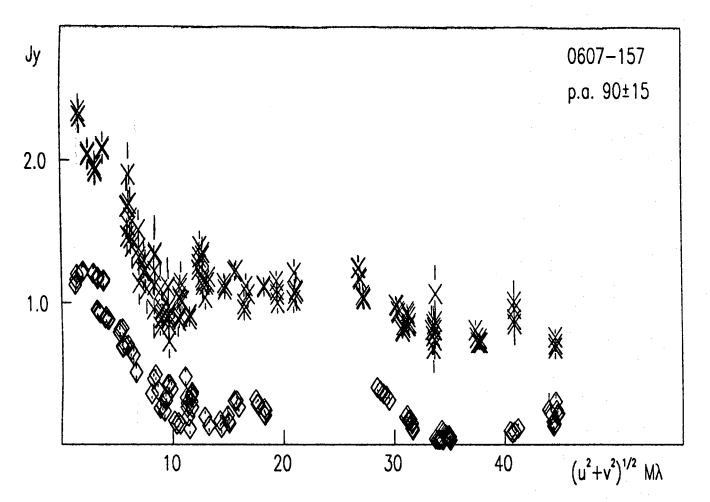


Fig. 9. Plot of amplitudes versus baseline length in position angle 90° for the source 0607-157. Diamonds refer to epoch 2.5 amplitudes and crosses to epoch 3.

implying two components separated by 3.3 mas at this p.a. If we assume that this component was not resolved during epoch 2 because it was too close to the core, the separation would be $<\!2.3$ mas (corresponding to the maximum observed baseline) during epoch 2. We therefore derive a lower limit to the proper motion of the component as $\mu \geq 0.2$ mas/year. This proper motion is in good agreement with that derived from the broadening of the nuclear component between epochs 1 and 2. The parameters in Table 3 indicate this proper motion with an expansion of about 1.4 mas in p.a. 120° of component C.

The structure of this source is confirmed by 5 GHz VLBI observations (Cerchiara, private communication).

0607–157: core-jet structure. The angular extension of the jet is about the same at all three epochs, but the core and jet components are brighter at epoch 3. Fig. 9 shows the amplitudes in position angle 90° from epoch 3 and epoch 2.5. In this plot a minimum is clearly visible at about $10M\lambda$. It is slightly displaced

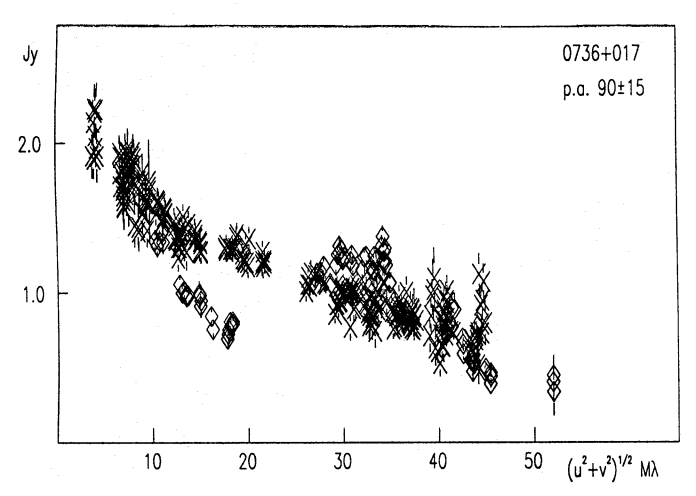


Fig. 10. Plot of amplitudes versus baseline length in position angle 90° for the source 0736+017. Diamonds refer to epoch 2 amplitudes and crosses to epoch 3.

between the two epochs, and corresponds to a separation, at position angle 90°, of $\theta_{90^\circ} \simeq 10$ mas for epoch 3 and $\theta_{90^\circ} \simeq 8.6$ mas for epoch 2.5. This implies a proper motion of $\mu \simeq 0.3$ mas/year. The parameters in Table 3 indicates this proper motion with a new component N separated by about 9 mas at p.a. 59°. In the previous observations it was not considered to be separate from the C component.

0723-008: asymmetric structure with a knotty jet extending more than 30 mas from the core in a northern direction. The epoch 3 map shows much more extended structure than the previous maps due to the better sensitivity and u-v coverage. Comparison of the amplitudes does not reveal any structural or flux density variation between the three epochs. The source was also observed at the epoch 2.5, and again these data do not show any variations. Because of the complex structure (Fig. 3) no gaussian fit is given for the extended components in Table 3. 0736+017: structure fitted with three components. During the first two epochs the variability was caused by changes in the flux densities and separation of two clearly identified components. In the epoch 3 map the two components can no longer be identified without ambiguity. We associate the eastern component of the epoch 2 map (A in Table 3) with the brightest component of the epoch 3 map and identify it with the core. The core flux density has increased while component B flux density has decreased. The change in the source structure is also clearly visible in Fig. 10 where the amplitudes along the source axis are plotted (p.a. 90°).

0859—**140**: structure fitted with three components. It appears quite symmetric at all epochs, but the extended structure in the N-S direction must be taken with caution. The source has not varied, even if the epoch 3 map shows much more detailed structure than the previous epochs. This is almost certainly due to better epoch 3 sensitivity. MERLIN observations at 408 MHz (Mantovani, private communication) show a compact core and two lobes aligned in the N-S direction.

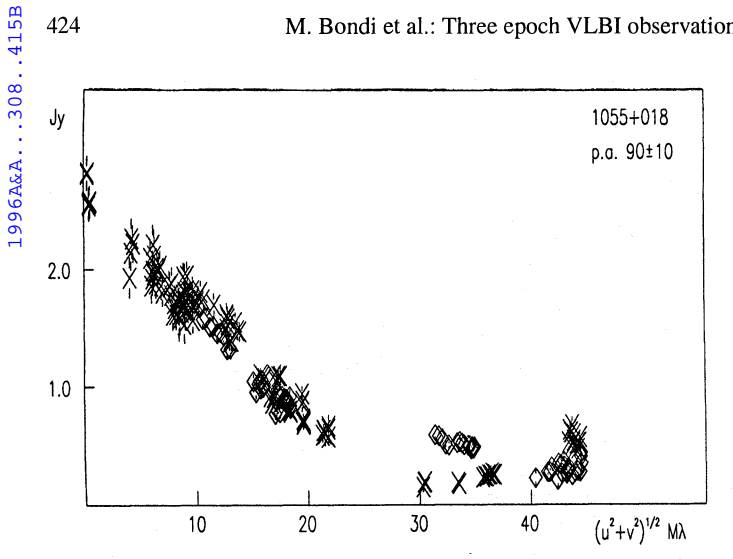


Fig. 11. Plot of amplitudes versus baseline length in position angle 90° for the source 1055+018. Diamonds refer to epoch 2.5 amplitudes and crosses to epoch 3.

1055+018: core-jet structure. The source did not vary between the first two epochs. Because of better sensitivity, epoch 3 reveals an extended component of 0.1 Jy at about 21 mas from the core in position angle -63° (N2 in Table 3). A jet, about 15 mas long, from the core towards this component is easily visible. Fig. 11 shows a plot of the amplitudes in position angle 90° for epochs 2 and 3. In the plot an amplitude minimum is clearly visible in epoch 3 at $b \simeq 34 M\lambda$. This corresponds to a component, also fitted from the map, at about 2.8 mas from the core in position angle -64° . This component (called N1 in Table 3) was not resolved from the core in the previous epochs. Component O (seen in the first two epochs) is now confused by this component. The data of epoch 2.5 confirm this gradual merging of an old and a new component.

On the arcsecond scale (Murphy, Browne & Perley 1993) 1055+018 shows a triple structure: a central bright compact component and two extended lobes in the N-S direction. The southern lobe is connected to the central core by a jet, but there is no hint of a jet towards the northern lobe.

1116+128: core-jet structure. This source did not vary between epochs 1 and 2. The variability observed between epochs 2 and 3 is mainly due to a flux density increase in the compact region (< 10 mas), now fitted with two components.

1127-145: core-jet structure. The core appears more compact than in previous epochs and shows a strong increase in flux density. This suggests that a new component may be emerging.

1510-089: core-jet structure. This source was a candidate for superluminal motion after the first two epochs. Epoch 3 does not confirm such an expansion. The observed variation is produced by a decrease of the core flux density.

1611+343: single compact component. No flux density or structural variations were detected in any of the three epochs.

1641+399 (3C 345): well known core-jet structure with extended emission. In epoch 2, the central region of the source was fitted with two components separated by 3.3 mas in position angle $\simeq -70^{\circ}$. In epoch 3, the map and the visibility data are fitted by a three component model: a compact core, a component at 2.5 mas in p.a. $\simeq -75^{\circ}$ and a component at 5.3 mas in p.a. $\simeq -67^{\circ}$. If we assume that the component 3.3 mas from the core in epoch 2 has moved to 5.3 mas in epoch 3, we derive a proper motion of $\mu \simeq 0.3$ mas/year in agreement with that found by Rantakyrö et al. (1992) at the same frequency.

1730–130: complex structure fitted with three components. The variability observed in this source is due to a large increase in the flux density of the central component suggesting that a new component in emerging. Parameters in Table 3 are mainly deduced from the visibility fitting. The map in Fig. 5 is strongly affected by side lobes.

2200+420 (BL Lac): single component extended in the N-S direction. Between the last two epochs, the flux density has decreased and the dimensions of the source have increased. We derive an expansion rate of $\mu \simeq 0.4$ mas/yr. Mutel et al. (1990) find, on a smaller scale, values of ~ 1 mas/year for different components resolved at higher frequencies.

2251+151 (**3C 454.3**): core-jet structure. The epoch 2 map was fitted with two components: a core (C) and a second component (A) at about 6.6 mas in p.a. $\simeq -62^{\circ}$ embedded in a lower surface brightness bridge. At epoch 3 map the core flux density has strongly increased and there is a new component at 4.0 mas in p.a. $\simeq -90^{\circ}$. Component A has not significantly changed its distance from the core. If we assume that the new component emerged from the nucleus between the last two epochs we derive a lower limit for the proper motion ≥ 0.3 mas/year compatible with the value measured by Pauliny-Toth et al. (1987).

6. Low frequency variability and superluminal motion

A comparison between flux density variability at 408 MHz and structural changes observed with VLBI observations at 18 cm is an alternative way to relate low frequency outbursts to either an extrinsic or an intrinsic origin.

From the 408 MHz light curves it is possible to derive the variability amplitudes and timescales in the period between VLBI observing epochs. From these, assuming that the variability is intrinsic, we can further calculate the brightness temperature (in the rest frame of the source) and hence the required Doppler factor for each source to avoid the inverse Compton catastrophe. We refer to the Doppler factors so obtained as the variability Doppler factor (δ_{var}) .

To calculate the Doppler factors from the 408 MHz light curves for each source, we examine the interval between the last two VLBI observing epochs (Fig. 12).

In this interval (\sim 1981 - 1988), it is usually possible to identify a flux density increase, a relative maximum and then a decrease (an "outburst") or a monotonic trend of flux density changes either increasing or decreasing. It may also happen that, superimposed on an "outburst" or a trend lasting few years there is more rapid variability (e.g. 1641+399). It should be kept in mind that the unknown quiescent level of a source, i.e. the relative contribution to the total flux density from the nonvari-

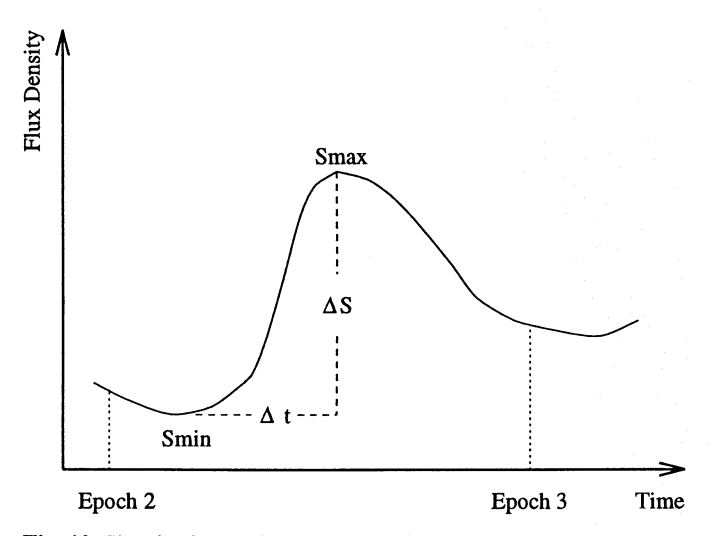


Fig. 12. Sketch of an outburst on a low frequency light curve.

able components, is a source of uncertainty in calculating the variability timescale, and that this is even more difficult at low frequencies where many "outbursts" with long timescales may overlap. Two extreme cases can be considered.

- 1. The variation is due to a transient component with maximum flux equal to the amplitude of the variation. The remaining flux of the source is assumed to belong to a stationary underlying component. On this assumption we take as a timescale (τ) the shorter of the two time intervals, between the maximum and the adjacent minima (Δt) : $\tau = \Delta t$.
- 2. No stable underlying component exists. The measured flux density at any time is a superposition of many outbursts, and the maxima are just the tops of the icebergs. In this case the timescale is defined as : $\tau = (S_{max}/\Delta S)\Delta t$.

Clearly, the first assumption leads to shorter timescales and the second assumption to longer ones. The real situation is likely somewhere in between these two hypothesis, so that we have arbitrarily chosen a level of half of flux density before the outburst as the quiescent level. Therefore, we define the peak flux density of an outburst S as the peak measured flux density of the outburst in the interval 1981 – 1988 minus half of the flux density measured before the outburst (or half of the flux density measured after the outburst in the case of a decline; see. e.g. Teräsranta & Valtaoja 1994). In the example sketched in Fig. 12, $S = S_{max} - S_{min}/2$ and $\Delta S = S_{max} - S_{min}$. It is important to note that the values of timescale are only slightly affected by the definition adopted for the quiescent level. The Doppler factors calculated using this method differ by less than 10% with those derived, for the same outbursts, adopting assumption 2. With this assumption, our definition of the timescale in the source frame is:

$$\tau_{burst} = \frac{S\Delta t}{\Delta S(1+z)} \tag{3}$$

Knowing τ_{burst} it is possible to calculate, using causality arguments, the maximum angular dimension of the bursting region as:

$$\theta_{burst} = \frac{2c\tau_{burst}}{D_L} (1+z)^2 \tag{4}$$

and the brightness temperature in the source's rest frame as:

$$T_{burst} = \frac{Sc^2}{2k\Omega\nu^2}(1+z) \tag{5}$$

 D_L is the luminosity distance, $\Omega = \pi \theta_{burst}^2/4$ is the solid angle corresponding to θ_{burst} , and ν is the observing frequency.

In order to avoid the inverse Compton catastrophe the plasmoids associated with the flux density outburst must be moving relativistically with a Doppler boosting factor given by:

$$\delta_{var} \simeq \left(\frac{T_{burst}}{10^{12}}\right)^{1/3} \tag{6}$$

The exponent in Eq. 6 depends on the geometry and the spectral index of the component (Blandford and Königl 1979). The value 1/3 is appropriate for a single shock component with spectral index $\alpha \sim 0$ (cf. Valtaoja et al. 1988). This value of δ_{var} is likely to be a lower limit to the true Doppler factor. In fact, Readhead (1994) has recently demonstrated that the intrinsic (i.e. not modified by relativistic effects) brightness temperatures in compact components of extragalactic radio sources is in the range $10^{10}-10^{11}$ K, well below the maximum inverse Compton limited brightness temperature of 10^{12} K.

We have calculated δ_{var} (Eq. 6) for sources that show 408 MHz variations in the interval of interest and for which the 18 cm VLBI observations show structural changes.

If the variations are intrinsic, the low frequency variability is a relic of high frequency outbursts, and the values of δ_{var} can be compared with the structure variations observed at 18 cm.

If we assume that the angle ψ between the line of sight and the true velocity direction is equal to $1/\gamma$ (where γ is the Lorentz factor), then β_{app} is maximum and, for $\beta \simeq 1$, we have $\beta_{app} \simeq \delta$. Thus, it is possible to obtain an estimate of the Doppler boosting factor required to explain the observed proper motion of the superluminal components, given by:

$$\delta_{kin} \simeq \beta_{app} = 47.4 \mu \frac{z}{1+z} \tag{7}$$

The results are shown in Table 4. The name of the source (column 1) has a flag identifying the spectral behaviour of the variability (as described in Padrielli et al. 1987): "C" for sources that are known to show variability events correlated over a wide frequency range, "U" for sources with activity uncorrelated between high and low frequencies with a minimum of variability in the intermediate frequency range ($\simeq 1 \, \text{GHz}$), and "L" for sources showing only variability in the low frequency range (< 1 GHz). Some sources are not classified due to a lack of multifrequency long period monitoring. Column 2 gives the outburst peak flux density after subtraction of a quiescent level. Columns 3 and 4 give the variability amplitude and the timescale of the variation, in the relevant interval, from the 408 MHz data. Column 5 shows the redshift (when a redshift was not available we have assumed a value of 0.5). Column 6 gives the brightness temperature in the source rest frame. Column 7 gives δ_{var} , calculated from the

426

Table 4. Doppler factors

Name		S	Δ S	Δ t	Z	T_{burst}	δ_{var}	δ_{kin}
		Jy	Jy	yr		° K		
0202+149		3.2	0.5	2.3	(0.5)	1.5 10 ¹³	2.5	≤1.3
0224+671		2.5	0.7	0.2	(0.5)	$4.8 \ 10^{15}$	16.9	\sim 5
0333+321		2.4	1.1	1.8	1.26	$6.5 \ 10^{14}$	8.7	≤4.3
0605 - 085	C	2.6	0.7	2.0	0.87	$1.2 \ 10^{14}$	4.9	≥4.4
1055+018	C	2.6	0.5	1.8	0.89	$7.6 \ 10^{13}$	4.2	≥ 2.3
		2.5	0.4	0.5		$6.8 \ 10^{14}$	8.7	
1127-145	U	3.9	1.2	1.0	1.19	$1.4 \ 10^{15}$	11.2	≤ 4.2
1510-085	C	1.9	0.6	1.6	0.36	$4.3 \cdot 10^{13}$	3.5	≤ 1.0
1611+343	L	2.6	1.6	2.6	1.4	$8.7 \cdot 10^{14}$	9.5	≤ 2.7
		1.6	0.6	0.5		$4.8 \ 10^{15}$	16.9	
1641+399	C	6.2	1.8	2.5	0.60	$1.1 \ 10^{14}$	4.8	5.8
		4.9	0.8	0.5		$7.4 \ 10^{14}$	9.0	
2200+420	C	1.9	1.1	3.5	0.07	$1.5 \ 10^{12}$	1.1	~ 1.2
2251+151	U+C	7.2	1.1	1.5	0.86	$1.8 \cdot 10^{14}$	5.7	6.6

408 MHz light curves (for sources showing 408 MHz variability on two different timescales both values are reported). Column 8 lists δ_{kin} , derived from the VLBI proper motions.

The two lower limits in δ_{kin} are due to the fact that a new component observed during epoch 3 was not observable in the previous epochs so that only a lower limit to the proper motion can be estimated. Upper limits in δ_{kin} are estimated from the quoted errors (3σ) for sources which did not show any structural variation.

The distribution of δ_{var} is quite peculiar: a number of values are $\simeq 4$, with the remaining value all > 8, with a broad distribution. The low values of δ_{var} are associated with 408 MHz bursts of low amplitude correlated with stronger bursts observed at higher frequencies, a spectral behaviour in agreement with the intrinsic model of variability. Among the sources showing these broad band, correlated bursts are the well known "bona fide" intrinsic variables (0605-157, 1055+018, 1510-089, 1641+399 and 2200+420) (Spangler et al. 1989). These δ_{var} are also compatible with the Doppler factors calculated from the structural variations at 18 cm.

On the other hand, the sources with $\delta_{var} > 8$ correspond to those having 408 MHz bursts with shorter timescales and generally stronger intensity, which are not correlated with events observed at higher frequencies. This is consistent with the fact that we do not see any structural variations compatible with such high Doppler factors from our maps, and implies that the 408 MHz variability producing such high δ_{var} must have an extrinsic origin.

The classification of the radio sources as "bona fide" intrinsic variables, variables only at low frequencies, or variables without correlation at high and low frequencies (respectively C, L, and U in Table 4), can be a bit misleading. What is more physically meaningful is to classify each burst according to its origin, since a source can have both intrinsic and extrinsic variations. This is the case for some of the "bona fide" variables (1055+018, 1510-089 and 1641+399) and may be the case for all the sources that have been classified as uncorrelated. For example, based on new low frequency data, we have been able to identify in the source 2251+151, previously classified as U, the relic of a high frequency variability event.

We therefore can conclude that two mechanisms are responsible for the variability observed in compact extragalactic radio sources: 1) an intrinsic mechanism due to the expansion of relativistically moving plasmoids emitting synchrotron radiation or to the propagation of shocks along a jet, and 2) an extrinsic mechanism due to refractive interstellar scintillation. Multifrequency monitoring of a sample of compact extragalactic radio sources shows that, in the majority of the sources, both phenomena are present. The intrinsic mechanism is responsible for most of the variability at high frequency and the extrinsic mechanism produces most of the low frequency variability.

7. Conclusions

Of the radio sources observed during a three epoch VLBI experiment carried out over about 8 years, 85% have shown significant variability. Some objects show flux density variations in one or more components without any significant change in the dimensions or separations between the components, while others show structural variations that can be identified with the motion of old components or with the birth of new ones. Some sources show variations which are so complex that neither of the aforementioned patterns can be recognized.

From a comparison of three epoch data taken in 1980.1, 1981.8, and 1987.9, we have found eight candidates for superluminal motion: 0224+671, 0316+413, 0605-085, 0607-157, 1055+018, 1641+399, 2200+420 and 2251+151. While some of these are well known superluminal sources (0316+413, 1641+399, 2200+420 and 2251+151; see Vermeulen and Cohen 1994 and references therein), other sources must be mapped at higher frequencies to confirm their superluminal nature.

Comparison between the VLBI structural variations at 18 cm and the flux density variations at 408 MHz over the same interval shows that for the majority of sources there is no correspondence between structural variations on the mas scale (δ_{kin}) and low frequency outbursts (δ_{var}) . Only in a minority of events $(0202+149,\ 0605-085,\ 1055+018,\ 1641+399,\ 2200+420$ and 2251+151)408 MHz flux density variations and the 18 cm VLBI structural variations are clearly related. These results reinforce the hypothesis that LFV in extragalactic radio sources is mainly due to an extrinsic mechanism affecting all compact (≤ 10 mas at 408 MHz) radio sources. As might be expected, the very compact intrinsic variables also show evidence for an extrinsic origin for some outbursts.

Acknowledgements. The authors are grateful to the European and US VLBI Networks, and to the Caltech Block-2 Correlator personnel for correlating the data. This research has made use of the NASA/IPAC Extragalactic Database (NED), which is operated by the Jet Propulsion Laboratory of the California Institute of Technology, under contract with the National Areonautics and Space Administration. MB acknowledges financial support from the European Union as an EU Fellow under contract CHBGCT920212.

References

Aller, H.D., Hughes, P.A., Aller, M.F., 1991, in: Miller R., Wiita P.J. (eds.) Variability of Active Galactic Nuclei, p. 172

Altschuler, R.D., 1989, Fund. Cosm. Phys., 14, 37

Blandford, R.D., Königl, A., 1979, ApJ, 232, 34

Bondi, M., Mantovani, F., Sherwood, W., Tzioumis, A., Venturi, T., 1994a, A&AS, 103, 365

Bondi, M., et al., 1994b, A&A, 287, 390

Fanti, C., et al., 1981, A&AS, 45, 61

Hewitt, A., Burbidge, G., 1987, ApJS, 63, 1

Marr, J.M., Backer, D.C., Wright, M.C.H., Readhead, A.C.S., Moore, R., 1989, ApJ, 337, 671

Marscher, A.P., Broderick, J.J., 1985, ApJ, 290, 735

Mitchell, K.J., et al., 1994, ApJS, 93, 441

Murphy, D.W., Browne, I.W.A., Perley, R.A., 1993, MNRAS, 264, 298 Mutel, R.L., Phillips, R.B., Su, B., Bucciferro, R.R., 1990, ApJ, 352

Padrielli, L., et al., 1986, A&A, 165, 53 (Paper II)

Padrielli, L., et al., 1987, A&AS, 67, 63

Pauliny-Toth, I.I.K., et al., 1987, Nat, 328, 778

Perley, R.A., 1982, AJ, 87, 859

Perley, R.A., Fomalont, E.B., Johnston, K.J., 1982, ApJ, 255, L93

Rantakyrö, F.T., Baath, L.B., Pauliny-Toth, I.I.K., Matveyenko, L.I., Unwin,S.C., 1992, A&A, 259, 8

Readhead, A.C.S., 1994, ApJ, 426, 51

Rickett, B.J., Coles, W.A., Burgois, G., 1984, A&A, 134, 380

Rickett, B.J., 1990, A&AR, 28, 561

Rickett, B.J., Quirrenbach, A., Wegner, R., Krichbaum, T.P., Witzel, A., 1995, A&A, in press

Romney, J.D., et al., 1984, A&A, 135, 289 (Paper I)

Schwab, F.R., Cotton, W.D., 1983, AJ, 88, 688

Shapirovskaya, N.Y., 1978, SvA, 22, 544

Spangler, S.R., Eastman, E.A., Gregorini, L., Mantovani, F., Padrielli, L., 1993, A&A, 267, 213

Spangler, S.R., Fanti, R., Gregorini, L., Padrielli, L., 1989, A&A, 209, 315

Stickel, M., Meisenheimer, K., Kühr, H., 1994, A&AS, 105, 211 Teräsranta, H., Valtaoja, E., 1994, A&A, 283, 51

Valtaoja, E., et al., 1988, A&A, 203, 1

Venturi, T., Readhead, A.C.S., Marr, J.M., Backer, D.C., 1993, ApJ, 411, 552

Vermeulen, R.C., Cohen, M.H., 1994, ApJ, 430, 467

Véron-Cetty, M-P, Véron, P., 1991, A catalogue of quasars and active nuclei 4^{rd} edition, ESO Scientific Report

This article was processed by the author using Springer-Verlag IATEX A&A style file version 3.